RAS Techniques and Instruments

RASTI **4,** 1–13 (2025) https://doi.org/10.1093/rasti/rzaf057
Advance Access publication 2025 November 19

A new broad-band atmospheric dispersion corrector for HROS-TMT

Manjunath Bestha [1,2]★ Thirupathi Sivarani,[1] Bachar Wehbe [3,4] Amirul Hasan,[1,5] Bharat Chandra P [1] Devika K Divakar,[6] Athira Unni [7] Parvathy Menon,[1,2] Arun Surya[1] and Pallavi Saraf[1,8]

[1]*Indian Institute of Astrophysics, Bangalore, P-560034, India*
[2]*Department of Applied Optics and Photonics, University of Calcutta, Kolkata, P-700106, India*
[3]*Instituto de Astrofísica e Ciências do Espaço, Universidade de Lisboa, Campo Grande, P-1749-016 Lisboa, Portugal*
[4]*Departamento de Física, Faculdade de Ciências, Universidade de Lisboa, Campo Grande, P-1749-016 Lisboa, Portugal*
[5]*Department of Physics and Electronics, Christ University, Bangalore, P-560029, India*
[6]*McDonald Observatory, University of Texas, Austin, P-78712, USA*
[7]*Department of Astronomy and Astrophysics, University of California, Santa Cruz, P-95064, USA*
[8]*Astronomy and Astrophysics division, Physical Research Laboratory, Ahmadabad, P-380058, India*

Accepted 2025 November 5. Received 2025 November 4; in original form 2025 May 1

ABSTRACT

Atmospheric dispersion causes light from celestial objects with different wavelengths to refract at varying angles as it passes through Earth's atmosphere. This effect results in an elongated image at the focal plane of a telescope and diminishes fibre coupling efficiency into spectrographs. We propose an optical design that incorporates a Rotational Atmospheric Dispersion Corrector (RADC) to address the broad-band dispersion for the multi-object mode of the High-Resolution Optical Spectrograph (HROS) on the Thirty Meter Telescope (TMT). The RADC corrects the dispersion across the entire wavelength range (0.31–1 μm), using Amici prisms optimized for over 90 per cent transmission efficiency and minimal angular deviation of the beam from the optical axis after dispersion correction. For enhanced accuracy, particularly in the blue region, we have, for the first time, implemented the Filippenko model in Zemax via a custom Dynamic-Link Library (DLL) file.

Key words: instrumentation: spectrographs – atmospheric effects – surveys – telescopes – instrumentation – atmospheric dispersion corrector.

1 INTRODUCTION

Broad-band observations play a key role in astronomical spectroscopic studies; for instance, they help study the detailed chemical abundances of astronomical objects in a single observation, such as stellar archaeology and exoplanet atmosphere characterization (C. Sneden et al. 2000; V. Hill et al. 2002; T. Sivarani et al. 2004; J. L. Birkby 2018; N. C. Santos et al. 2020; P. Saraf et al. 2023; A. Bandyopadhyay et al. 2024; S. Rukdee 2024; M. Bestha et al. 2025). However, these observations from the ground are affected by atmospheric dispersion. This phenomenon occurs when light from celestial objects passes through Earth's atmosphere and gets refracted. This leads to elongated images on the focal plane of telescopes (C. G. Wynne & S. P. Worswick 1986). For spectroscopic observations, it causes wavelength-dependent input losses at slit or fibre and reduces the overall spectrograph efficiency.

In slit-based spectrographs, slit losses can be minimized by aligning the slit along the parallactic angle (G. P. Szokoly 2005). One effective method to mitigate dispersion in fibre-fed spectrographs is to feed the pupil image into the fibres. However, feeding the pupil image directly into the fibre in crowded fields can allow multiple objects to enter a single fibre. Therefore, dispersion correctors are extensively used in fibre-fed spectrographs to correct atmospheric dispersion.

Upcoming large telescopes, such as the Extremely Large Telescope (ELT)[1] (E. Oliva et al. 2018; P. Padovani & M. Cirasuolo 2023) and the Thirty Meter Telescope (TMT)[2] (A. C. Phillips et al. 2016), face challenges in correcting atmospheric dispersion across the wide field of view, primarily due to the need for large correction optics. To address this challenge, a segmented Atmospheric Dispersion Corrector (ADC) design concept was proposed for the Large Sky Area Multi-Object Fibre Spectroscopic Telescope (LAMOST), with diameters of 1.75 and 1.22 m for the North and South telescopes, respectively (D.-q. Su, P. Jia & G. Liu 2012). However, constructing and maintaining segmented ADCs that align with the curvature of the telescope's focal plane becomes challenging[3] as the field of view increases.

Therefore, this paper presents the optical design of an ADC based on a widely utilized concept, tailored for single-object dispersion correction within individual narrow fields. The proposed ADC is intended to provide dispersion-corrected light to the High-Resolution Optical Spectrograph (HROS) (T. Sivarani et al. 2022), a second-

[1]https://elt.eso.org/
[2]https://www.tmt.org/
[3]Similar to the increase in design complexity of segmented mirror telescopes, as the primary aperture size increases.

★ E-mail: bestha95@gmail.com

Table 1. This table summarizes key specifications of the Thirty Meter Telescope (TMT) and the High-Resolution Optical Spectrograph (HROS).

Specifications of TMT and HROS instruments	
Primary mirror diameter	30 m
Secondary mirror diameter	3.1 m
Focal plane curvature radius	3.01 m
Field of view size	20 arcmin (equivalent to 2.616 m)
Plate scale	2.18 mm/1 arcsec
Wavelength range	0.31–1 μm
Blue channel wavelength range	0.31–0.45 μm
Red channel wavelength range	0.44–1.0 μm
MOS spectral resolution	25 000
Fibre size for MOS mode	1 arcsec

generation instrument proposed for the TMT. HROS covers a wavelength range from 0.31 to 1 μm and supports various operational modes, including Multi-Object Spectroscopy (MOS). In MOS mode, up to six objects can be observed simultaneously, utilizing 1 arcsec fibres to achieve a spectral resolution of $R = 25\,000$. By blocking subsequent echelle orders, the slit can accommodate up to forty objects (T. Sivarani et al. 2022; M. Bestha et al. 2023). The ADC is integrated within the fibre positioners responsible for feeding light to the spectrograph (F. M. Zerbi et al. 2014; M. Bestha et al. 2024). The details of TMT and HROS are discussed in Section 2.

Atmospheric dispersion correction is typically achieved using one of two common types of correctors in astronomical observations: Linear Atmospheric Dispersion Correctors (LADCs) (G. Avila, G. Rupprecht & J. M. Beckers 1997) and Rotational Atmospheric Dispersion Correctors (RADCs) (C. G. Wynne 1996). An LADC operates by translating one of two identical, oppositely oriented prisms along the optical axis within a converging beam to counteract atmospheric dispersion. However, LADCs introduce a lateral shift in the beam that varies with the zenith angle, which can lead to throughput losses, especially in systems with stationary fibre inputs (M. Bahrami & A. V. Goncharov 2011; A. Rakich 2021). To overcome this limitation, the RADC design, featuring counter-rotating Amici prisms, is incorporated into the fibre positioner, achieving simultaneous correction of both dispersion and beam deviation, thereby enhancing spectrograph efficiency. In this context, the term 'beam' refers to the polychromatic light with a reference wavelength of 0.45 μm.

2 OVERVIEW OF THE THIRTY METER TELESCOPE AND HIGH-RESOLUTION OPTICAL SPECTROGRAPH

The Thirty Meter Telescope (TMT) (A. C. Phillips et al. 2016; T. Sivarani et al. 2022; M. Bestha et al. 2023) is an alt-azimuth Ritchey-Chrétien (RC) telescope planned for construction on Mauna Kea, Hawaii. It consists of a concave hyperboloid primary mirror (M1), a convex hyperboloid secondary mirror (M2), and a flat tertiary mirror (M3). The primary mirror has a diameter of 30 m, which is achieved by assembling 492 hexagonal segments. The secondary mirror has a diameter of 3.1 m (see Table 1). At the final focus, the telescope delivers a f/15 beam with a plate scale of 2.18 mm/1 arcsec and a focal plane diameter of 2.616 m, corresponding to a field of view of 20 arcmin. The focal plane has a radius of curvature of 3.01 m, which results in a non-telecentric beam. On-axis, TMT achieves an image quality with a geometric radius of ~ 10 μm. However, due to astigmatism, this degrades to ~ 730 μm at an off-axis field point located at (7 arcmin, 7 arcmin), since Ritchey-Chrétien (RC) telescopes are not inherently corrected for astigmatism (M. C. Rocha & A. V. Goncharov 2022). The effect is illustrated by the TMT focal plane spot diagram (Fig. 1). The off-axis point corresponds to a radial distance of ≈ 9.9 arcmin from the field centre, yielding a total field of view of about 20 arcmin in diameter.

The TMT is designed to host both adaptive optics-assisted instruments and seeing-limited instruments mounted on either side of the Nasmyth platform. One of the second-generation instruments, the HROS (T. Sivarani et al. 2022), is seeing-limited and aims to leverage TMT's large aperture even under moderate seeing conditions. It supports operation using direct slit-fed and fibre-fed modes, offering three resolutions: high-resolution ($R = 100\,000$), standard mode ($R = 50\,000$), and multi-object spectroscopy (MOS) mode ($R = 25\,000$), with a wavelength coverage of 0.31–1.0 μm (T. Sivarani et al. 2022; M. Bestha et al. 2023).

The MOS mode utilizes fibre positioners to collect the light from the focal plane to feed the spectrograph. The design of the positioner incorporates an ADC along with fore optics, comprising a collimator, a camera, a dichroic, and a pick-off mirror. This integrated assembly is called the Atmospheric Dispersion Correction System (ADCS), and each positioner arm has its own ADCS.

The pick-off mirror redirects incoming light toward the collimator using small tip and tilt adjustments. For on-axis targets, the mirror is set at a 45° angle to the chief ray. For off-axis targets, the angle is adjusted by $\pm\Delta\theta$, where $\Delta\theta$ is the offset between the on-axis and off-axis directions (M. Bestha et al. 2024). The redirected light then passes through the ADC, which corrects for atmospheric dispersion, and is split into two wavelength bands using a dichroic: 0.31–0.45 μm (blue channel) and 0.44–1.0 μm (red channel), as listed in Table 1. A 0.01 μm overlap is included in the red channel since the typical dichroic cannot split the light exactly at the desired boundary. The light is then coupled into optical fibres using micro lenses.

3 ADC DESIGN CONSIDERATIONS

Achieving high radial velocity (RV) precision requires tight control over atmospheric dispersion residuals. To support an RV stability of 10 cm s^{-1}, residual dispersion must be maintained below 0.1 arcsec across the 0.38–0.78 μm wavelength range (B. Wehbe et al. 2020a). Assuming a linear relationship between RV precision and residuals, a stability target of 1 m s^{-1} allows residuals up to 1 arcsec. Therefore, the required residual correction for our design is not difficult and does not impose severe constraints on the system's RV performance.

To date, ADCs compatible with the HROS working wavelength have not been reported, which spans from 0.31 to 1.0 μm. A reported three-material dispersion corrector using FK5, LLF2, and Fused Silica provides over 90 per cent transmission from 0.33 to 1.3 μm (S. Eisenberg & K.-L. Shu 1985). However, the material LLF2 has a transmission of ≈20 per cent at 0.31 μm for a 10 mm thickness,[4] which is significantly lower than required, making it not suitable for our purposes. Therefore, designing the ADC for HROS-MOS requires the following:

(i) Selection of an optimal material combination for the Amici prism to achieve a transmission efficiency greater than 90 per cent across the 0.31–1.0 μm working wavelength range.

(ii) Ensuring effective dispersion correction in the near ultraviolet region (below 0.33 μm).

[4] https://refractiveindex.info/?shelf=specs&book=HIKARI-optical&page=LLF2

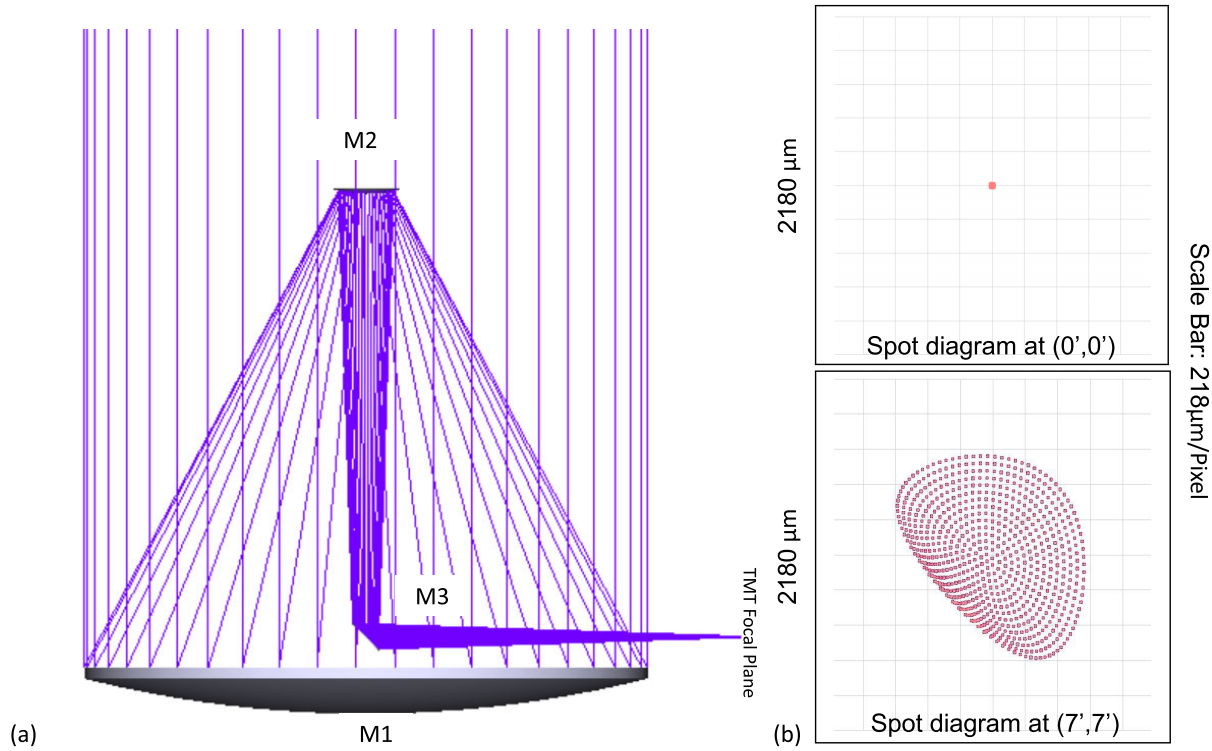

Figure 1. (a) The TMT optical layout, and (b) The spot diagrams for a reference wavelength of 0.45 µm. The top panel shows the spot diagram for the on-axis position, while the bottom panel displays the spot diagram for the off-axis position.

(iii) Maintaining dispersion corrected light within a 1 arcsec fibre diameter by controlling the beam's positional deviations as a function of zenith angle. This prevents introducing large movements of the fibre at the end of the fibre positioner (M. Bestha et al. 2024).

The limited availability of suitable materials and the need to correct for a higher dispersion towards the near UV region make designing an ADC for the HROS-MOS mode challenging.

4 IMPLEMENTATION OF THE FILIPPENKO 1982 MODEL IN ZEMAX

We have used ZEMAX to design and analyse the optical system. The default atmospheric model in ZEMAX is based on the work of C. Y. Hohenkerk & A. T. Sinclair (1985), accessed through the atmospheric surface feature option available in Zemax (LLC 2011). However, P. Spanò (2014) highlighted that this built-in model underestimates atmospheric dispersion, particularly in the blue spectral region. To mitigate this issue, we implemented the A. V. Filippenko (1982) model, which has been extensively validated against on-site measurements of atmospheric dispersion (B. Wehbe, A. Cabral & G. Ávila 2020b). This implementation was achieved by developing a Dynamic Link Library (DLL) file using C++ programming and incorporating it as a user-defined surface within Zemax. The source code and the DLL file are available in GitHub.[5]

For the design of TMT-HROS, we adopted atmospheric parameters mentioned in J. J. Wang et al. (2020) for the site Mauna Kea, at Hawaii, with a temperature of 276.15 K, relative humidity of 20 per cent, and a pressure of 614 mbar. These parameters were then input into the newly implemented Filippenko model in Zemax to simulate the atmospheric conditions at the TMT-HROS site.

5 DESIGN OF THE ROTATIONAL ADC FOR HROS-TMT

Although the elongation of spots due to dispersion for the entire wavelength range of HROS is 3.631 arcsec, the dispersion for the blue and the red channels is 2.219 and 1.526 arcsec, respectively. However, individually correcting the dispersion for both channels would require two separate correctors within the fibre positioner of the HROS-MOS mode. To avoid the need for two separate correctors that can be integrated within the positioners, we have designed a single corrector capable of working in the HROS passband.

First, we have modelled the Thirty Meter Telescope (TMT) with a primary mirror diameter of 30 m and a secondary mirror diameter of 3.1 m. The conic constants, representing hyperbolic mirrors, are −1.0009530 and −1.3182280, respectively. The radii of curvature are −60000.0 and −6227.680 mm. The distances between M1 and M2, and M2 and M3, are −27093.750 and 23593.750 mm, respectively. A fold mirror (M3) diverts the beam to the Nasmyth platform at a distance of 19999.786 mm, resulting in an effective focal length of 450 m and an f/15.[6] The optical layout of the instrument and image quality of the TMT design are depicted in Fig. 1.

The design of ADCS includes a pick-off mirror of ≈ 5 arcsec diameter, which can tilt to direct the non-telecentric f/15 beam from the TMT focal plane, either on-axis or off-axis, to the doublet lens collimator, with an effective focal length of 291 mm, which

[5]https://github.com/bestha95/Filippenko1982_DLL/

[6]https://www.tmt.org/; https://www.nao.ac.jp/en/research/telescope/tmt.html

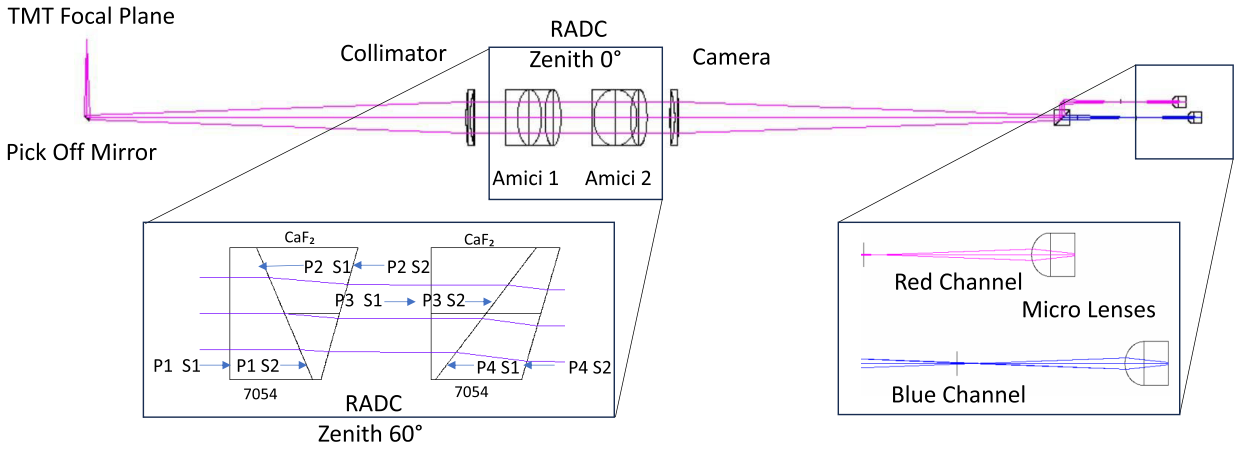

Figure 2. Optical layout of the atmospheric dispersion corrector (ADC), where the Amici prisms are counter-rotated by 90° at Zenith 0°, along with the fore optics. P1, P2, P3, and P4 prisms belong to both Amici prisms. Here, S denotes a surface, and S1 and S2 represent surface 1 and surface 2 of the prisms, respectively. In Amici 1, S1 and S2 correspond to P1, where S2 of P1 is S1 of P2, and S2 of P2 is the last surface of Amici 1. Similarly, in Amici 2, S2 of P3 is S1 of P4, and S2 of P4 is the last surface of Amici 2. The first inset shows the ADC at a Zenith angle of 60°, incorporating flint glass Nikon-7054 and crown glass Ohara-CaF_2. The second inset displays the micro lens for the red and blue channels, which converts the f/15 beam to f/3.

Table 2. Abbe number and internal transmittance (T) values at 0.31 and 1 μm for the subset of glasses selected from the customized glass catalogue used during the optimization process. These materials were taken from Zemax inbuilt catalogues (such as Schott and Ohara) and a few additional materials from Nikon (2021). Only glasses with sufficiently high transmission were included. Transmittance values are given as dimensionless fractions (per 10 mm thickness).

Glass name	Abbe number	T(0.31 μm)	T(1 μm)
Nikon 7054	54.70	0.9650	0.9990
Nikon 5859	59.47	0.9800	0.9980
F_SILICA	67.82	1.0000	1.0000
LITHOSIL-Q	67.83	0.9996	0.9997
S-FSL5	70.24	0.8900	0.9980
S-FSL5Y	70.35	0.9540	0.9980
N-FK5	70.41	0.9545	0.9990
FK5	70.41	0.9502	0.9987
S-FPL51Y	81.14	0.8900	0.9980
Nikon 4786	86.78	0.9900	0.9980
CaF_2	94.99	1.0000	1.0000
LITHOTEC-CaF_2	95.23	0.9992	0.9996
NICF-V	95.26	0.9980	0.9980

collimates the dispersed beam, and then traverses through the ADC. As discussed in Section 1, an RADC is employed instead of an LADC to correct dispersion and deviations induced by the corrector through additional optimization to the prism surface tilts. The RADC comprises two doublet prisms, also known as Amici prisms, each consisting of two circular prisms (P1, P2, P3, P4, respectively) as shown in Fig. 2.

The prisms were modelled in Zemax using tilted surfaces. A custom catalogue was created to identify the optimal materials for the prisms, which consist of materials with transmission efficiencies ranging from ≈ 90 per cent to 100 per cent across a wavelength range of 0.31 to 1 μm. Materials are taken from Zemax inbuilt catalogues, such as Schott and Ohara glass catalogues, and a few materials are taken from Nikon (2021). Table 2 provides the list of materials in the custom catalogue. The transmission efficiencies of glass materials were calculated for a thickness of 10 mm as described in equation (1) derived from the Beer-Lambert law.

$$T_{\rm n} = T_{\rm o}^{\frac{d_{\rm n}}{d_{\rm o}}}, \tag{1}$$

where $T_{\rm n}$ is the transmission for the new thickness, $T_{\rm o}$ is the transmission for the original thickness (as provided in the vendor's data sheet), $d_{\rm n}$ and $d_{\rm o}$ are the new and original material thicknesses, respectively.

The prism materials, apex angles, and counter-rotation angles of the Amici prisms were optimized using the `CENY`, `GLCX`, `GLCY`, and `DIFF` operands of Zemax in the merit function. Specifically, `CENY` tracks the Y-coordinate of the image centroid, while `GLCX` and `GLCY` assess the global X and Y positions of rays, and `DIFF` calculates the difference between operands, ensuring minimized deviations. This optimization process used the multiconfiguration editor and Hammer optimization in Zemax.

From the optimization, we identified that Nikon 7054 combined with CaF_2 from our custom catalogue as the most suitable material combination for the prisms, exhibiting over 95 per cent transmission (per 10 mm thickness) over the 0.31–1.0 μm range (see Fig. 3). The apex angles of the four individual prisms were determined such that the second prisms (P2, P4) corrected the deviation caused by the first prisms (P1, P3) within the Amici prisms. Consequently, (P1, P4) and (P2, P3) are using identical materials but oriented in reverse directions. The individual prisms have distinct surface tilts as mentioned below; the reason for the distinct surface tilts is explained in the Section 6.2.

(i) P1: $S_1 = 0°,\ S_2 = -23.122°$
(ii) P2: $S_1 = -23.122°,\ S_2 = 15.695°$
(iii) P3: $S_1 = 0°,\ S_2 = 37.524°$
(iv) P4: $S_1 = 37.524°,\ S_2 = 16.224°$

Here, P stands for Prism and S for Surface. The apex angle is calculated as $|S_2 - S_1|$, where S denotes a surface, and S_1 and S_2 refer to tilt angles of surface 1 and surface 2 of the prisms, respectively. The two Amici prisms are then counter-rotated to cancel dispersion. The optimized parameters are provided in Table 3.

Subsequently, a camera with specifications identical to the collimator focuses the dispersion-corrected beam exiting the ADC. The geometric spot diagrams before and after dispersion correction at the

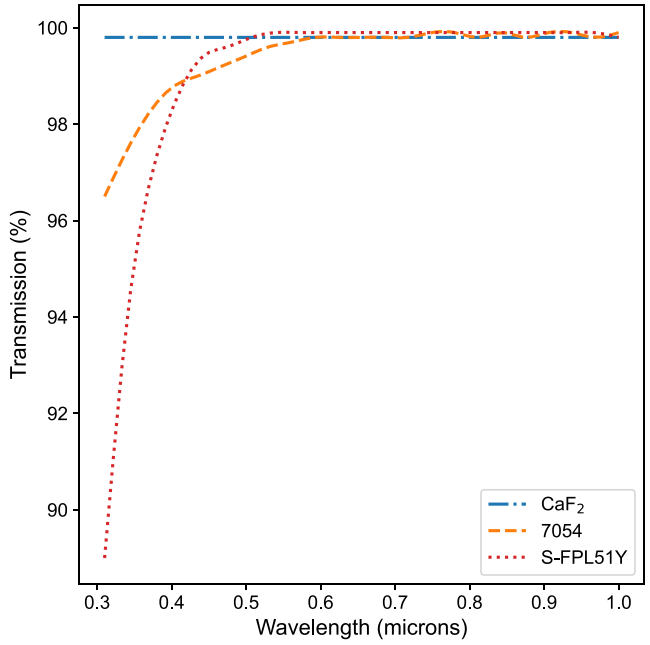

Figure 3. Transmission of materials used in designing the ADC (Nikon-7054 and CaF_2), as well as the collimator and camera (S-FPL51Y), for a thickness of 10 mm.

Table 3. Specifications of the atmospheric dispersion corrector, collimator, camera, and micro lens.

Atmospheric dispersion corrector	
Diameter	30 mm
Materials	Nikon 7054 & CaF_2
Apex Angles of P1, P2, P3, and P4	23.122 °, 38.807°, 37.524°, 21.3°
Counter rotation angles of Amici-prisms at zenith angles 0°, 20°, 40°, 60°	90°, 78.331°, 61.986°, 1.672°
Collimator and Camera	
Diameter	30 mm
Effective focal length	291 mm
Materials	S-FPL51Y & Nikon 7054
Micro Lens	
Semi diameter	3.6 mm
Radius of curvature	3.6 mm
Materials	Nikon 7054

TMT focal plane are shown in Figs 4 and 5, respectively. As shown in Fig. 4(a), before dispersion correction, the on-axis spot sizes for each wavelength are very small, limited by the geometric aberrations of the RC design. After passing through the collimator and camera, the spots broaden due to spherical and chromatic aberrations, as shown in Fig. 5(a). For the off-axis case, illustrated in Fig. 4(b), the spots are dominated by astigmatism, and their sizes further increase due to the aberrations from the collimator and camera. Moreover, the tilted surfaces in the optical system alter the astigmatism predominantly (W. J. Smith 2023), causing the spots to appear stretched (see Fig. 5b).

Additionally, a dichroic[7] is placed in the converging beam to separate the light into blue and red channels. The red channel is subsequently folded by a plane mirror to maintain the beam path within the fibre positioner. With an ≈ f/3 for both on-axis and off-axis objects across all zenith angles, the light is directed into both channels through microlenses made of Nikon 7054, positioned 33 mm from the camera focus. The geometric spots of both channels on the fibre are shown in Fig. 6. As shown, the image size at the pupil position (before the micro lens focus) increases from blue to red. This trend arises from the axial colour of the micro lens, where the refractive index variation with wavelength causes shorter wavelengths to focus closer to the micro lens than longer wavelengths, resulting in better image quality for the blue channel and a progressively larger blur toward the red. For the off-axis case, the image at the pupil position appears perturbed since the micro lens was designed for the on-axis field. This distortion arises from the change in the solid angle (numerical aperture) of the off-axis fields, which alters the shape of the off-axis image at pupil position (T. P. Johnson & J. Sasian 2020). We adopted a slightly larger 500 μm fibre at an f/3 instead of the 436 μm fibre to simplify the calculation and illustration. Therefore, at an f/3, the plate scale is 0.5 mm/1 arcsec.

6 ANALYSIS

Upon completing this design, we sought to validate whether it met our requirements. We performed dispersion residual calculations, beam deviation analyses, throughput calculations, and tolerance analyses to validate this design, which are detailed in this section.

6.1 Residuals

As discussed in Section 3, the residuals relevant to our design requirements are minimal. Nevertheless, we aimed to demonstrate the residual dispersion present in our design.

Before measuring the residuals, we validated the performance of the Filippenko (1982) model by computing the atmospheric dispersion at the TMT focal plane using ray tracing in Zemax. The linear displacement between rays at different wavelengths, measured relative to a reference wavelength, was converted into an angular scale using the plate scale. We compared results with those from a Python-based implementation of the same model (B. Wehbe et al. 2020b) under identical atmospheric conditions. The difference was 0.0001 arcsec, which is negligible as it is very small compared to the maximum dispersion at zenith angle 60° of HROS working wavelength coverage (≈ 3.631 arcsec) as shown in Fig. 7(a), and well within the HROS requirements.

Subsequently, the collimator and camera were replaced with paraxial lenses to eliminate the dispersion contributions from the transmission elements, ensuring that only the ADC residual dispersion was computed. The residuals evaluated before the micro lens at an f/15 as a function of zenith angle, wavelength, and counter-rotation angle of the Amici prisms. They remain within 0.25 arcsec across the HROS working wavelength range, as depicted in Fig. 7(b). As shown, the residual dispersion after correction exhibits a non-linear

[7]Since a dichroic with a cutoff wavelength near 0.45 μm is currently unavailable (https://www.asahi-spectra.com/opticalfilters/astronomy_dichroic.asp), a plane mirror at 45° embedded within a 15 mm silica cube is used as an alternative dichroic element. In this configuration, the tilted mirror is used to reflect light into the reflection channel, while the cube transmits the remaining light into the transmission channel.

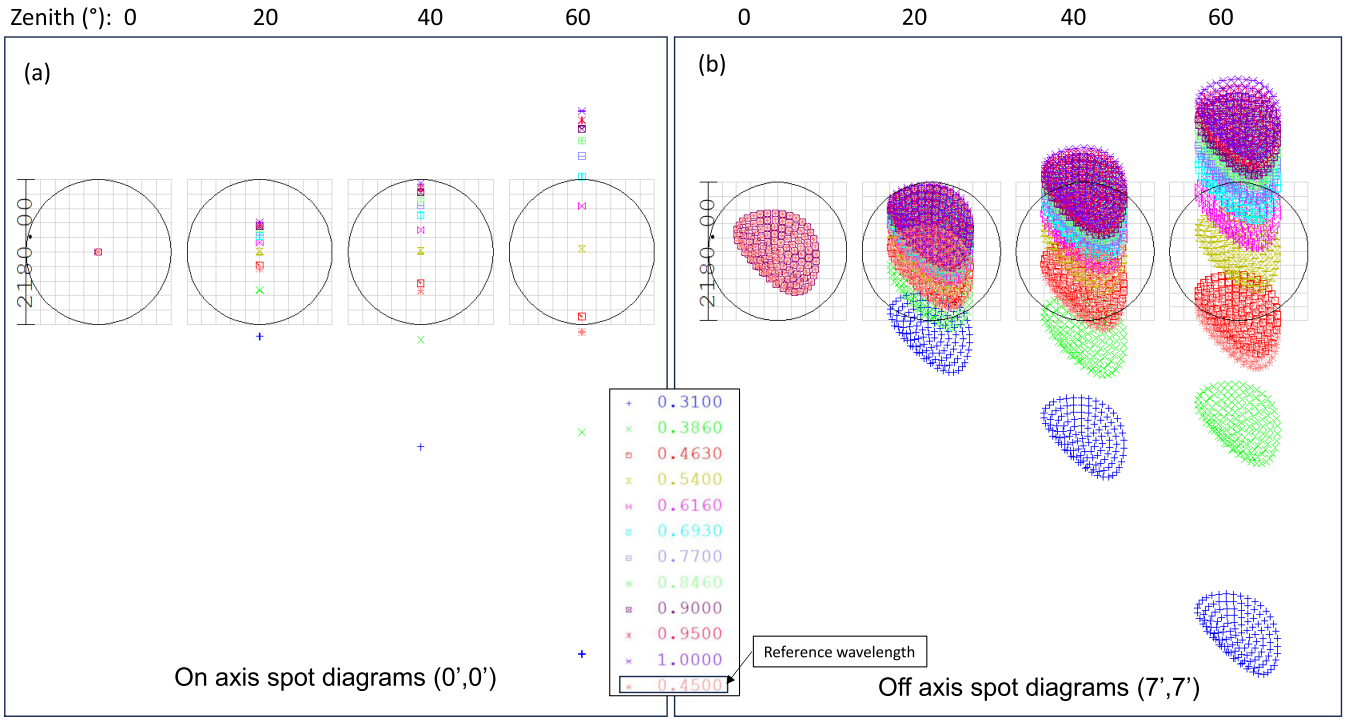

Figure 4. The image quality on the TMT focal plane. The circle represents a 1 arcsec fibre, corresponding to 2180 microns in linear scale at an f/15. (a) Spot diagrams of on-axis objects at different zenith angles without dispersion correction, where aberrations are minimal. (b) Spot diagrams of off-axis objects at different zenith angles without dispersion correction, where astigmatism predominantly affects image quality.

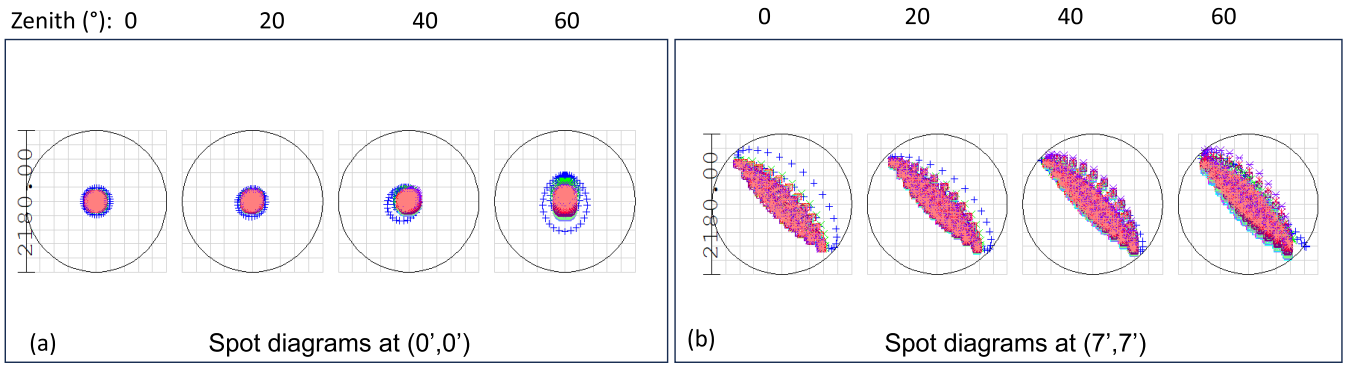

Figure 5. The image quality on the TMT focal plane. The circle represents a 1 arcsec fibre, corresponding to 2180 μm in linear scale at an f/15. (a) Spot diagrams of on-axis objects at different zenith angles after the dispersion correction. (b) Spot diagrams of off-axis objects at different zenith angles after the dispersion correction.

shape, due to the anomalous dispersion characteristics of the ADC glass materials (D. Kopon, L. M. Close & V. Gasho 2008). This arises because the net dispersion curve of the corrector does not perfectly match the atmospheric dispersion over the wavelength range (D. Greggio et al. 2020). None the less, these residuals remain within the requirements of HROS-ADC.

6.2 Deviations

In principle, LADCs work by altering the incident angle of rays on the movable prism as a function of the zenith angle to correct atmospheric dispersion. Conversely, RADCs function by changing the incident angle of rays relative to the prism normal, depending on the rotation of the Amici prisms. In LADCs, the beam deviations introduced by the first prism are offset by the second prism. In RADCs, a strategy involves using two different types of glass for the prisms, which exhibit varying dispersions but share the same refractive index at a specific wavelength (M. Bahrami & A. V. Goncharov 2011). Initially, we designed the ADC using identical Amici prisms, which corrected the atmospheric dispersion, resulting in residuals of 0.08 arcsec over the 0.31–1.0 μm range, demonstrating good performance. However, after correction, the polychromatic beam is deviated by

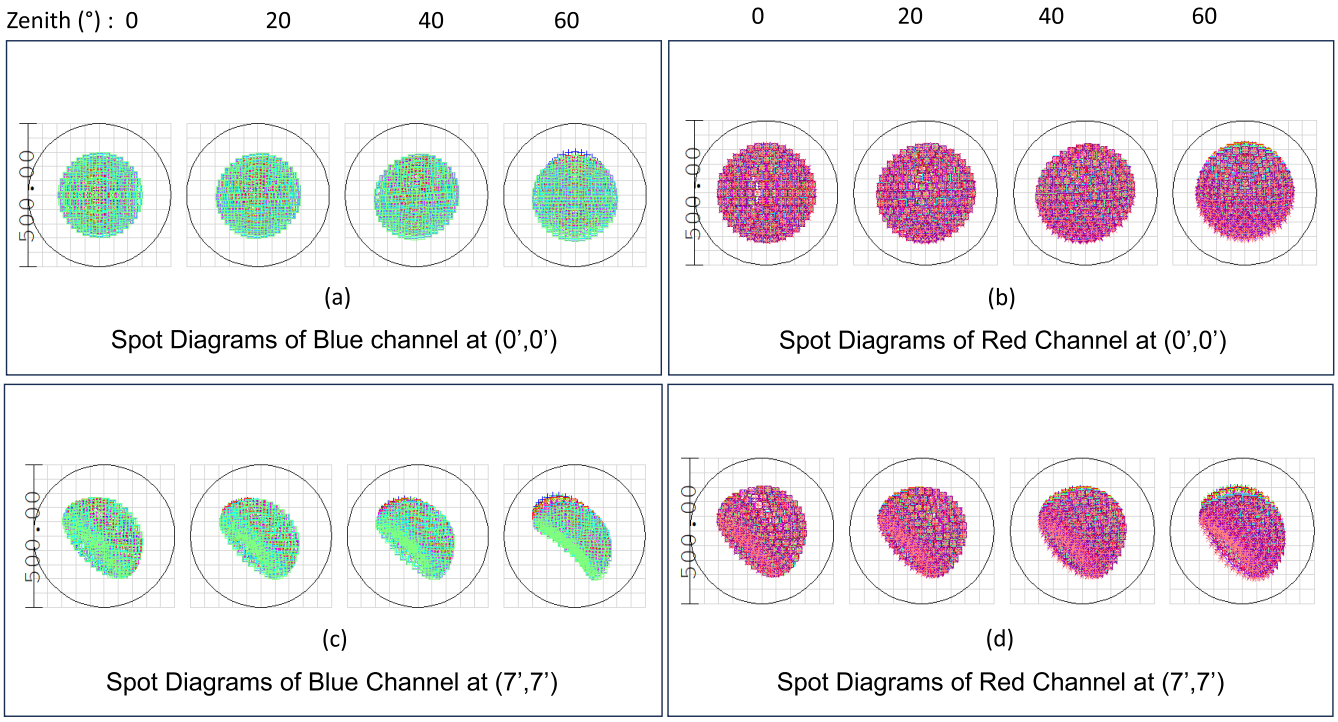

Figure 6. The image quality of dispersion-corrected light after passing through the micro lens onto a 1 arcsec fibre, corresponding to 500 μm in linear scale at an ≈ f/3 across different zenith angles. (a) Spot diagram of the on-axis object in the blue channel. (b) Spot diagram of the on-axis object in the red channel. (c) Spot diagram of the off-axis object in the blue channel. (d) Spot diagram of the off-axis object in the red channel.

up to 17 arcsec at a zenith angle of 60°, which corresponds to 38 mm in linear scale at the collimator focal plane for an f/15 beam. These deviations are caused by atmospheric refraction and the ADC itself, and they vary with both zenith angle and prism counter-rotation angles. The large deviation at higher zenith angles arises because the dispersion curves of the selected materials differ significantly, as shown in Fig. 8.

This substantial deviation was assessed using the ray tracing option in Zemax. The methodology involved calculating the distance between the position of the reference wavelength (0.45 μm) at zenith 0° and its positions at other zenith angles on the focal plane after dispersion correction. In this case, achieving maximum throughput requires displacing the fibre along the beam deviation direction, which closely coincides with the dispersion (parallactic) direction. However, this is challenging due to the significant beam deviation. To address this issue and avoid displacement of the fibre, tilts of outer surfaces of the Amici prisms were optimized, then the deviations were reduced to 0.16 arcsec, ensuring the beam remains well within the 1 arcsec of the fibre as shown in Fig. 9. Consequently, the displacements can be regarded as negligible.

6.3 Throughput

The geometrical image analysis (IMA) tool in `ZEMAX` and the `PyZDDE` Application Program Interface (API) (I. Sinharoy 2014) were used to estimate the geometric throughput for both on-axis and off-axis objects within a 1 arcsec fibre. The analysis was performed using image size settings of 15 and 3 mm based on the f-ratio of the beam. This analysis was conducted for the entire HROS working wavelength range, with and without dispersion correction.

The methodology for calculating geometrical throughput involved calculating the seeing for each wavelength using the relationship among seeing, Fried's parameter, and wavelength, as described in equation (2). We considered a seeing of 0.7 arcsec at a reference wavelength ($\lambda_{\rm ref} = 0.45$ μm) and computed seeing at different wavelengths. Using that, we created 2D Gaussian profiles, which were then convolved using `fftconvolve` from the SciPy library P. Virtanen et al. (2020) to perform fast convolution with the extracted geometrical position-based intensities obtained from the IMA tool. This process generated images of seeing-included geometric spots for different zenith angles before and after dispersion correction (see Fig. 10). The final results were multiplied by a 1 arcsec python-simulated circular aperture to account for the fibre size. The Fried parameter is given by;

$$r_0\,(\mathrm{m}) = \frac{0.98 \times \lambda\,(\mathrm{m}) \times 206265}{\mathrm{FWHM}_{\rm seeing} \times \text{plate scale}\,(\mathrm{m\,arcsec^{-1}})}, \tag{2}$$

where r_0 is the Fried parameter, representing the atmospheric coherence length. The constant 0.98 is empirical, 0.45 μm (0.45×10^{-6} m) is the reference wavelength, and 206265 is a factor for converting radians to arcseconds. The term $\mathrm{FWHM}_{\rm seeing}$ represents the full width at half maximum of the seeing disc at the reference wavelength (D. Giggenbach 2011).

The 2D Gaussian function is given by;

$$I(x, y) = \frac{\exp\left(-\left(\frac{(x-x_0)^2}{2\sigma_x^2} + \frac{(y-y_0)^2}{2\sigma_y^2}\right)\right)}{2\pi\sigma_x\sigma_y}, \tag{3}$$

where I is a function of displacement (x, y) relative to the origin (x_0, y_0). The parameters σ_x and σ_y represent the standard deviations of the distribution in arcseconds.

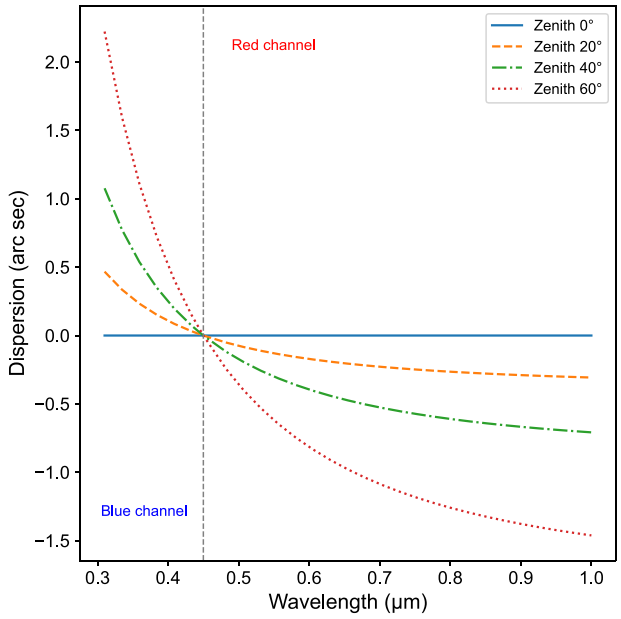

(a) The dispersion at the telescope focal plane computed before correction at different zenith angles

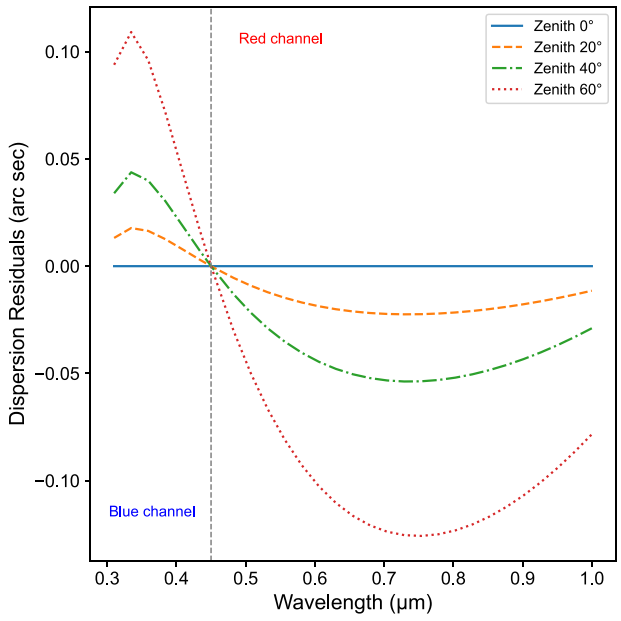

(b) The dispersion residuals after correction computed before the micro lens at different zenith angles by replacing the collimator and camera with paraxial lenses.

Figure 7. The figure depicts the dispersion before and after correction across the HROS working wavelength range at different zenith angles, modelled using the Filippenko (1982) framework in Zemax.

In Fig. 10, the panel (a) illustrates the decrease of intensity along the dispersion direction on the blue side (high dispersion) and its increase on the red side (low dispersion), while panel (b) shows the same images after correcting the dispersion within the 1 arcsec fibre before entering the micro lenses.

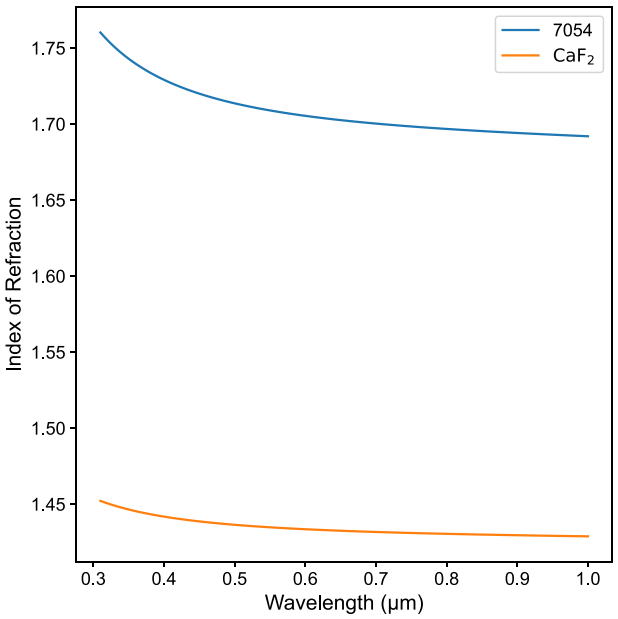

Figure 8. The dispersion curves of materials apart from each other, which are used in designing the ADC (Nikon-7054 and CaF_2).

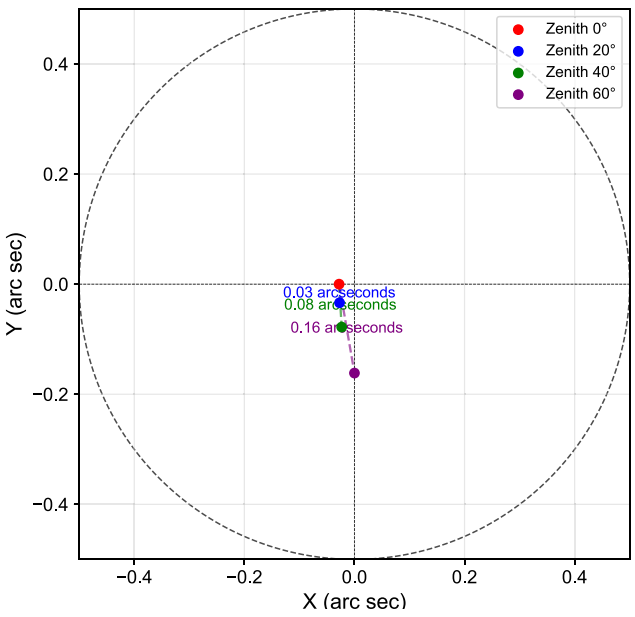

Figure 9. The figure shows a 1 arcsec fibre represented by a circle, with dots in different colours corresponding to the position of a reference wavelength (0.45 μm) at various zenith angles, as labelled in the image. The movement of the dots within the fibre illustrates the effect of deviation after the dispersion correction. It also demonstrates that the maximum deviation of the wavelength at 0.45 μm remains within the 1 arcsec fibre after the dispersion has been corrected.

The percentage of geometric throughput (% GT) is computed using the following equation:

$$\% \, \mathrm{GT} = \left(\frac{\mathrm{OPI}}{\mathrm{IPI}} \right) \times 100, \tag{4}$$

where IPI (Input Intensity) represents the sum of intensity before multiplication by the 1 arcsec circular aperture, while OPI (Output

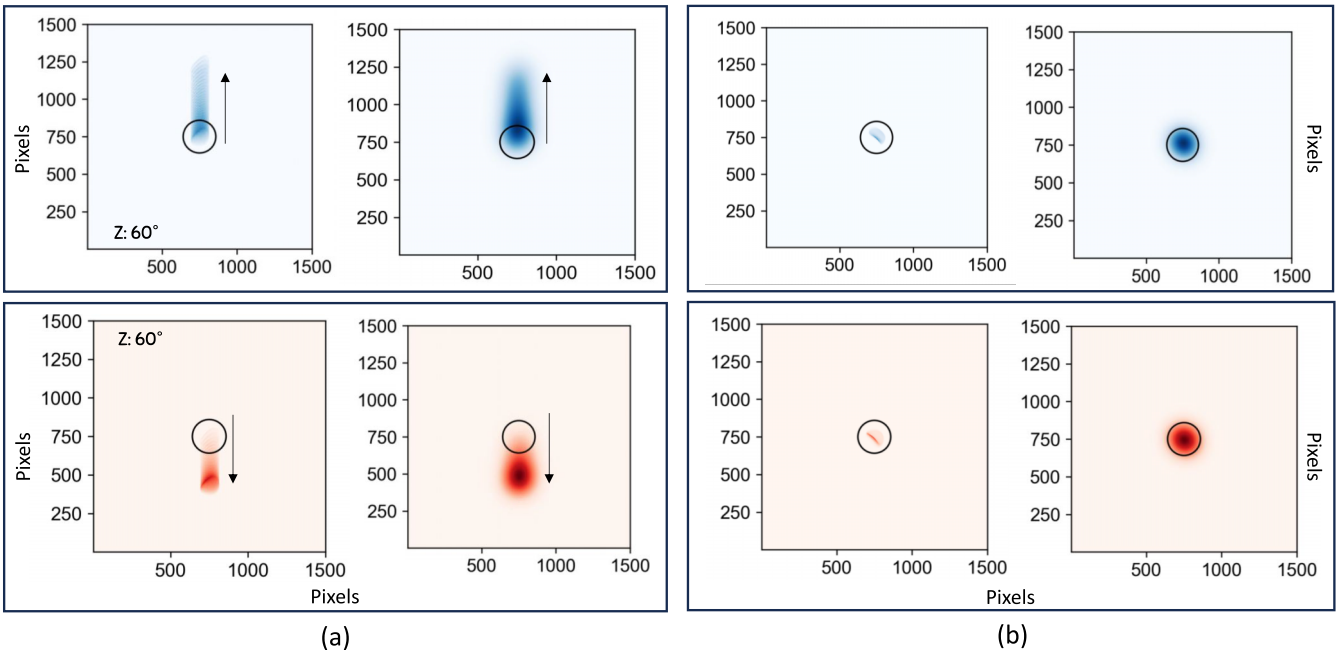

Figure 10. The figure illustrates aberrated off-axis spots at the reference wavelength (0.45 μm), positioned at the centre. The blue and red colours represent the blue and red channels of the wavelength coverage, respectively. The scale of the above image is 218 pixels per 1 arcsec. At an f/15 beam, 1 arcsec = 2.18 mm, while at an f/3 beam it corresponds to 0.5 mm. The black circle and arrow represent the 1 arcsec fibre and the direction of atmospheric dispersion, respectively. (a) Before the dispersion correction, the first column displays spot diagrams without atmospheric seeing, while the second column presents seeing-included images at the telescope focal plane. (b) After the dispersion correction, the first column shows spot diagrams without atmospheric seeing, whereas the second column illustrates seeing-included images at the fibre.

Intensity) represents the sum of intensity after multiplication by the 1 arcsec circular aperture.

Using this methodology, percentages of geometrical throughput for different zenith angles for an on-axis object, both before and after dispersion correction, are obtained. However, aberrations such as astigmatism affect the off-axis throughput, which is more prominent in RC telescopes and leads to signal loss at the fibre. To estimate its effect on % GT, the instrument's position was adjusted to analyse image quality over a (7 arcmin,7 arcmin) field of view. To account for the curvature of the TMT focal plane (sag = 279.214 mm over a (7 arcmin,7 arcmin) field), the ADCS at the off-axis position was repositioned to match the focal coordinates $(x, y, z) = (912, 912, -279.214)$ mm, corresponding to a distance of 19720.786 mm from M3 along the optical axis and 912 mm along each of the two perpendicular axes, ensuring that the off-axis focal surface coincides with the ADCS during throughput evaluation (M. Bestha et al. 2024). The off-axis images were then evaluated, including the impact of atmospheric seeing. The results of % GT from these analyses are presented in Figs 11 and 12. The plots show a significant increase in throughput after dispersion corrections. At a Zenith angle of 0°, the on-axis % GT is ≈ 75 per cent and off-axis % GT is ≈ 68 per cent at 0.31μm. At a Zenith angle of 60°, both on-axis and off-axis % GT were initially 0 per cent at 0.31μm, but after correction, on-axis % GT increased to 73 per cent and off-axis % GT to 65 per cent.

As shown in Figs 11 and 12, the maximum throughput occurs at the reference wavelength, as it lies closest to the optical axis after dispersion correction, and this is computed before the micro lens. These calculations assume the fibre is positioned at the reference wavelength location, ensuring coverage across the entire HROS working wavelength range. However, if the fibres in both channels are offset relative to their current positions, the maximum throughput of the wavelength will shift accordingly. Also, due to the non-linear nature of the dispersion correction, dips can be seen on the bluer side and around 0.72 μm in the on-axis plot (see Fig. 11b), where the corrected dispersion dominates over the optical aberrations. However, a similar trend is not observed in the off-axis plot (see Fig. 12b), where the optical aberrations dominate over the corrected dispersion.

To calculate the input signal entering the spectrograph from a 1 arcsec fibre, we considered factors, including the system's polishing quality of reflective elements (pq) which is the product of reflectivity of M1, M2, M3, and the pick-off mirror, Fresnel input-output losses (f_l), lens misalignment errors (m_e), and focal ratio degradation (FRD). The typical values assumed are $pq = 0.92$, $f_l = 0.92$, $m_e = 0.98$, and FRD = 0.90. These values account for simple spectrograph design throughput estimation as given in G. Avila & C. Guirao (2017). The transmission of high OH fibre (t_f) over 20 m was calculated using the attenuation as a function of wavelengths provided by Thorlabs[8] using equation (5). Furthermore, the transmission of the lenses (10 mm thickness) and prisms (50 mm thickness) within the system as a function of wavelength was also considered. The final calculation of the fibre output is illustrated in equation (6).

$$T_{\rm km} = 10^{-\alpha/10}, \quad T_{\rm fibre} = T_{\rm km}^{L/1000}, \tag{5}$$

where α is the fibre attenuation in dB km^{-1}, L is the fibre length in m, $T_{\rm km}$ is the transmission for 1 km of fibre, and $T_{\rm fibre}$ is the total

[8] https://www.thorlabs.com/Images/TabImages/FG_UGA_LGA_UCA_LCA_UEA_LEA_Attenuation_Data_2.xlsx

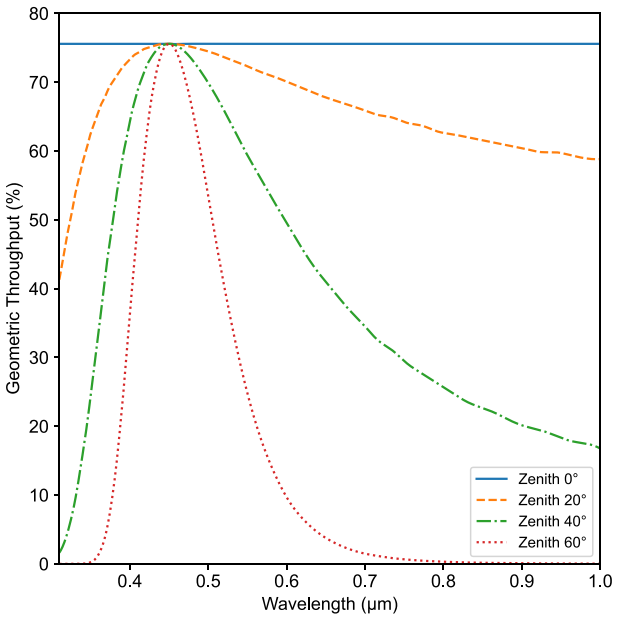

(a) Before the dispersion correction

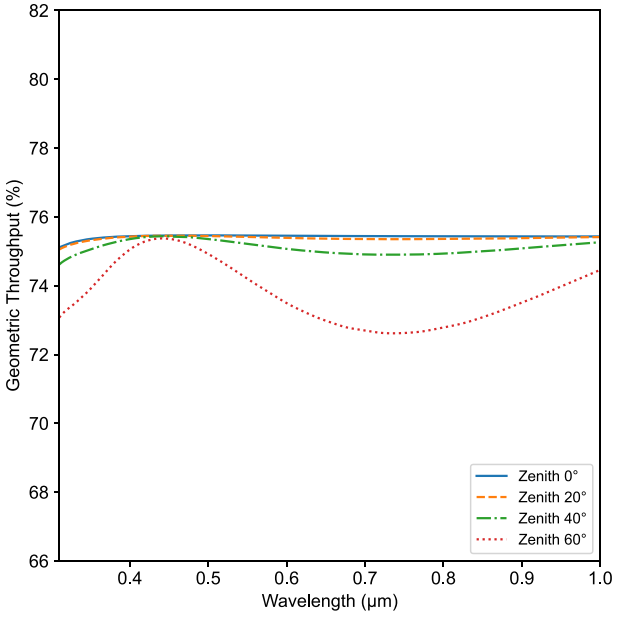

(b) After the dispersion correction

Figure 11. The geometric throughput across the HROS working wavelength range for the on-axis object at different zenith angles, estimated before splitting into channels.

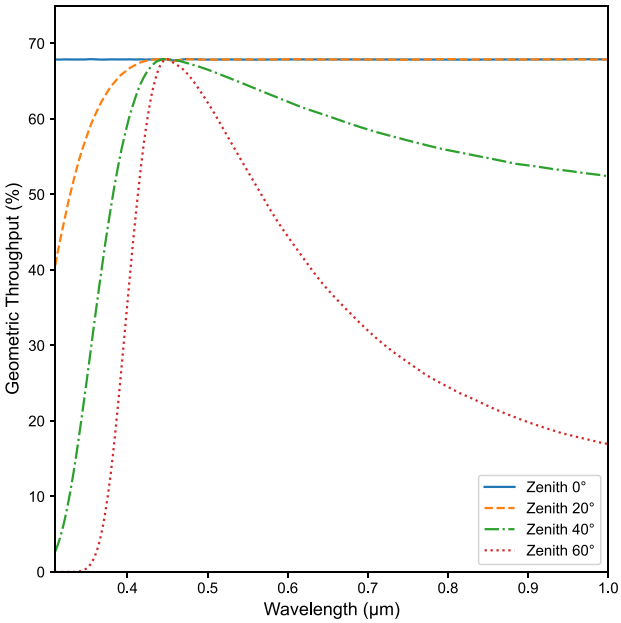

(a) Before the dispersion correction

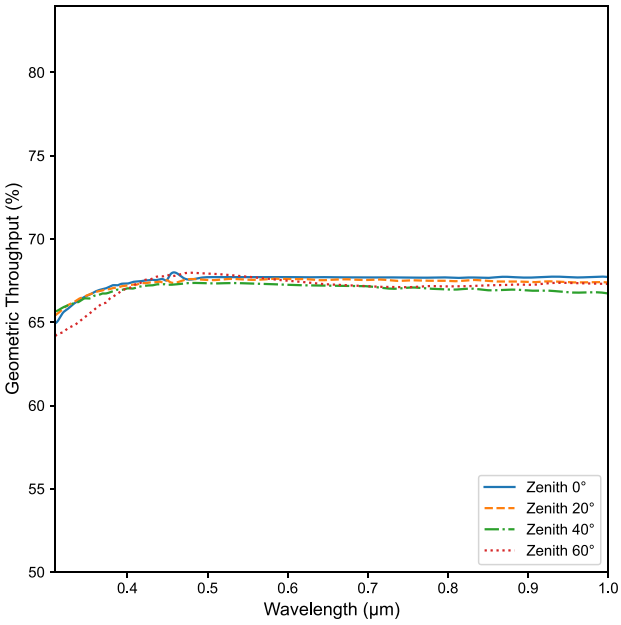

(b) After the dispersion correction

Figure 12. The geometric throughput across the HROS working wavelength range for the off-axis object at different zenith angles, estimated before splitting into channels.

transmission through a fibre of length L.

$$I_{\text{in}}(\lambda, Z) = pq \cdot f_l \cdot m_e \cdot \text{FRD} \cdot f_t(\lambda) \cdot t_{fa}(\lambda) \cdot \%\,\text{GT}(\lambda, Z). \tag{6}$$

In this expression, $I_{\text{in}}(\lambda, Z)$ is the input efficiency to the spectrograph, dependent on wavelength λ and zenith angle Z. The term $t_f(\lambda)$ denotes the fibre transmission, $t_{fa}(\lambda)$ transmission of fore optics (excluding dichroic and micro lens) and ADC, and $\%\,\text{GT}(\lambda, Z)$ represents the geometric throughput.

The input efficiency to the spectrograph, as a function of wavelengths and zenith angles, has significantly increased for the on-axis object after dispersion correction. At Zenith 60°, the efficiency was zero before the correction but improved to above 45 per cent at 0.31μm after the correction. The results are presented in Figs 13(a) and (b).

In the above efficiency calculations, the optical performance of the micro lens and dichroic was not considered, as the influence of atmospheric dispersion on throughput is not seen clearly at its pupil position, where aberrations such as spherical and axial chromatic

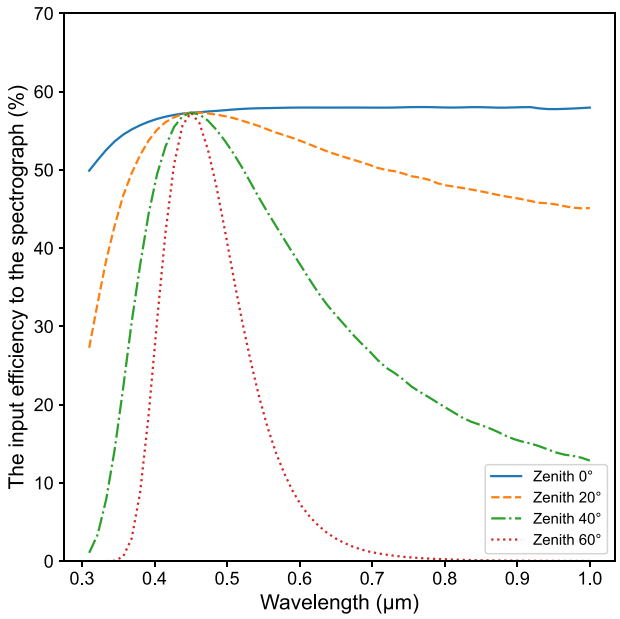

(a) Before the dispersion correction

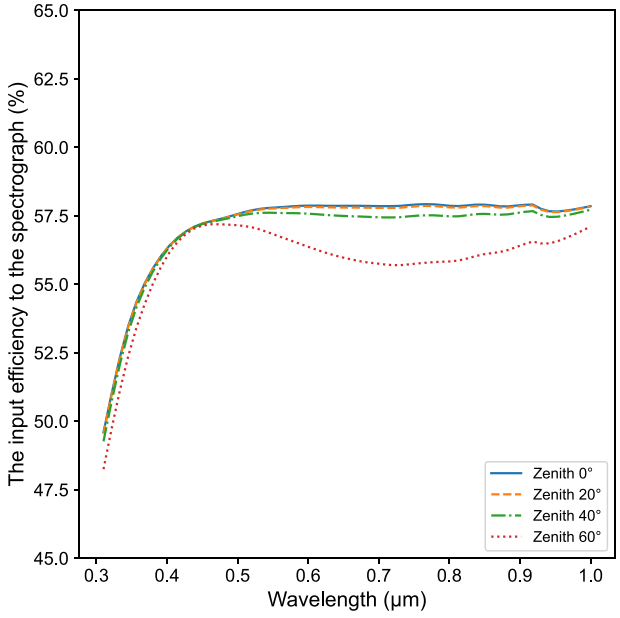

(b) After the dispersion correction

Figure 13. The total throughput entering the spectrograph across the HROS working wavelength range, as estimated by accounting for the transmission efficiency of the dichroic and micro lens.

aberration are present. The image at pupil position is considered to ensure uniform illumination across the fibre (G. Avila 2012). The input efficiency to the spectrograph was estimated using the percentage geometric throughput (% GT) at the pupil position, incorporating a dichroic transmission of 90 per cent, and the micro lens transmission across the full wavelength range, corresponding to lengths of 15 and 10 mm, respectively, along with the other parameters used in the previous efficiency calculation. The input efficiency to the spectrograph with a dichroic and micro lens is shown in Fig. 14, the efficiency decreases for both channels away

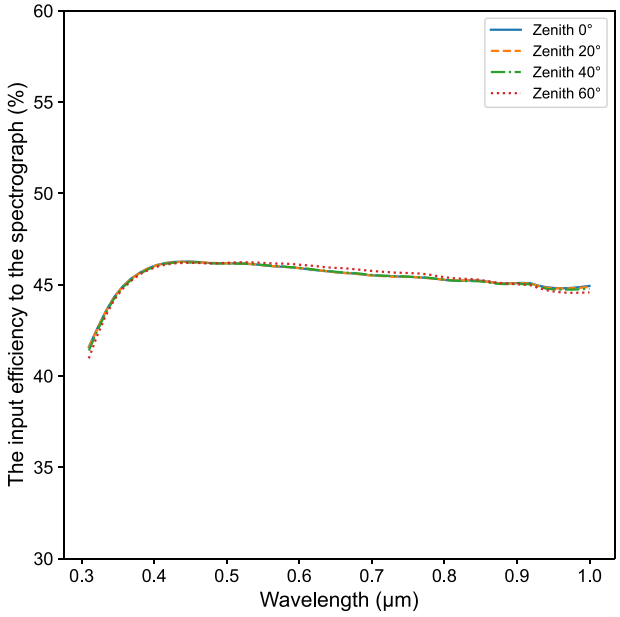

Figure 14. The total throughput entering the spectrograph across the HROS working wavelength range, as estimated by considering the optical effects of the micro lens.

from the reference wavelength. The reduction on the blue side is mainly due to the transmission losses of the optical elements, while the decrease on the red side is due to axial colour. The latter can be mitigated either by positioning the fibre at the focal plane of the micro lens or by employing aspheric lenses (M. Parvathy et al. 2025). A local peak is observed near 0.7 μm at a zenith angle of 60° as the residual wavelengths act as off-axis field points for the micro lens. Around this wavelength, the corrected rays lie farther from the optical axis, creating a pupil coma (T. P. Johnson & J. Sasian 2020). This redistribution of rays produces a smaller geometric spot, which increases the throughput.

6.4 Tolerance analysis

This section discusses the sources of errors that influence the system throughput, primarily governed by the spot radius. Since HROS is seeing-limited and designed for a stability goal of 1 m s^{-1}, the manufacturing requirements are comparatively less stringent than those of adaptive optics (AO)-assisted instruments (C. Cunningham et al. 2008; R. A. Simcoe et al. 2016; R. J. Harris et al. 2025).

For the design up to the camera focal plane in the ADCS, tolerance analysis was performed using the Zemax tolerancing tool, which evaluates surface-related (manufacturing) and element-related (alignment) errors individually. The tool employs a Monte Carlo approach to estimate the impact of perturbations in the optical system. The primary objective of tolerance analysis was to ensure that spot radius variations induced by tolerances remain confined within the 1 arcsec fibre footprint specified in the requirements.

For manufacturing tolerances, we considered the tolerances listed in Table 4 for each surface in the design, from the TMT focal plane to the camera focus. These included thickness deviations of 0.1 mm, radius deviations of ±1 per cent, and x- and y-tilt angle errors of up to 0.5° (M. Bestha et al. 2023). Tilts of the prism surfaces, in particular, affect the effective apex angle. We found that the average

Table 4. The table presents the manufacturing and alignment tolerances considered for the ADC and fore optics design. Manufacturing tolerances include tilts, decentre, radius, and thickness deviations, while the alignment tolerances account for decentre, tilt, and rotational errors of the optical elements. The 2 arcmin of parallelism error is included by assigning a ±1 arcmin alignment tilt tolerance along each axis.

Manufacturing (Surface)		Alignment (Element)	
X&Y-Decentre	±1 mm	X&Y-Decentre	±1 mm
X&Y-Tilt	±1 arcmin	X&Y-Tilt	± 1 arcmin
Radius	±1 per cent	Rotation angle	± 0.5°
Thickness	± 0.1 mm		

image quality decreases by ≈5 per cent under the applied surface tolerances.

For alignment tolerances, we applied rotational perturbations of ±0.5° to the Amici prisms and x- and y-tilts of 1 arcmin, decentre errors of ±1 mm, as summarized in Table 4. These perturbations were introduced one element at a time-collimator, Amici 1, Amici 2, and camera-while keeping the others fixed. On average, the spot diagrams changed by ≈10 per cent under these alignment perturbations.

Although such large decentre values are not typically required during instrument alignment, since they can displace the beam outside the stable fibre and cause significant light loss, they were intentionally adopted in HROS-ADC tolerance analysis. This approach probes the robustness of the design and evaluates image quality under exaggerated alignment errors. By comparison, AO-assisted instruments generally require much tighter tolerance budgets.

A potential source of concern in high-precision radial velocity spectrographs is the accuracy of melt data, i.e. refractive index inhomogeneities and temperature-dependent variations introduced during glass production. Melt data-related residuals of up to 0.15 arcsec in atmospheric dispersion correction have been reported for the material combination PBL6Y + N-PK51[9] (0.42–0.78 μm) when the originally optimized prism apex angles are used. These residuals can be reduced by re-optimizing the prism apex angles (B. Wehbe et al. 2019), which is crucial for ultrastable instruments aiming for $\sim 10\,\mathrm{cm\,s^{-1}}$ radial velocity precision. In the HROS-MOS case, with a stability requirement of $1\,\mathrm{m\,s^{-1}}$ (corresponding to a tolerance of 1 arcsec), such deviations are not expected to be a dominant limitation. Therefore, melt data were not considered in this analysis.

7 CONCLUSION

In this paper, we presented the optical design of an ADC tailored for a broad wavelength coverage, ranging from 0.31 to 1 μm. The design mitigates dispersion, bringing throughput at a Zenith angle of 60° across the working wavelength to nearly equal the Zenith angle of 0°. This improvement enhances the overall efficiency of the spectrograph while ensuring beam deviations are constrained to keep the light within a 1 arcsec fibre. Although the ADCS was specifically designed to meet the requirements of the MOS mode for the HROS on the TMT, the material combination of Nikon 7054 and CaF_2, which provides over 95 per cent transmission for a thickness of 10 mm, renders it suitable for other applications.

[9]Based on reported melt and temperature coefficients, the Nikon 7054-CaF_2 pair exhibits refractive-index stability similar to that of the N-PK51-PBL6Y combination. Both pairs show low-to-moderate sensitivity ($\Delta n \sim 10^{-5}$–10^{-6}; $\mathrm{d}n/\mathrm{d}T \sim 7$–$10 \times 10^{-6}\ \mathrm{K}^{-1}$). (D. B. Leviton, B. J. Frey and T. J. Madison 2015; Nikon 2021; SCHOTT 2022; Ohara Corporation 2024).

One key part of this work is modifying the atmospheric model within Zemax, enabling a more precise ADC design that effectively addresses dispersion and beam deviations. Following correction, the beam deviations are confined to a minimal area with a radius of only 0.16 arcsec, ensuring the required performance.

To validate the robustness of the design, a tolerance analysis was performed using Zemax to simulate potential manufacturing and alignment errors. The results indicate that while the average image quality decreased by 10 per cent due to manufacturing and alignment tolerances, this degradation does not significantly impact the throughput to the spectrograph. By convolving the increased spot size due to system perturbations with atmospheric seeing, we demonstrated that the resulting image quality remains within the required specifications.

Furthermore, micro lenses made from Nikon 7054 glass were added to change the system's focal ratio from an f/15 to ≈ f/3, ensuring efficient coupling into the fibre and uniform illumination across its core.

In conclusion, the proposed ADC design, with its new combination of materials, corrections, and robust tolerance analysis, addresses the stringent requirements of HROS-TMT. Its flexibility and high throughput make it a promising solution for both on-axis and off-axis observations using seeing-limited fibre-fed spectrographs.

ACKNOWLEDGEMENTS

We thank the optical engineer, Mr Bernard Delabre, suggestion to use Nikon glass materials. We also thank the anonymous reviewer(s) for their constructive comments and suggestions, which have helped us improve the quality of the manuscript. We thank the Department of Science and Technology, India TMT team, the Indian Institute of Astrophysics, and the University of Calcutta for their unwavering support throughout this work.

CONFLICT OF INTEREST

The authors declare no conflict of interest.

DATA AVAILABILITY

The source code and DLL file for the Filippenko (1982) model are included in the GitHub[5] repository. Data information, sourced from the Thorlabs website[8], is also provided. Zemax designs and Zemax-Python interfacing codes will be shared upon request to the corresponding author, with permission from India-TMT.

REFERENCES

Avila G., 2012, in McLean I. S., Ramsay S. K., Takami H., eds, Proc. SPIE Conf. Ser. Vol. 8446, Ground-based and Airborne Instrumentation for Astronomy IV. SPIE, Bellingham, p. 84469L

Avila G., Guirao C., 2017, in ASpekt 2017. St. Niklausen, Switzerland, https://spectroscopy.wordpress.com/wp-content/uploads/2009/05/aspekt-2017.pdf (Accessed December 2025)

Avila G., Rupprecht G., Beckers J. M., 1997, in Ardeberg A. L., ed., Proc. SPIE Conf. Ser. Vol. 2871, Optical Telescopes of Today and Tomorrow. SPIE, Bellingham, p. 1135

Bahrami M., Goncharov A. V., 2011, Opt. Express, 19, 17099

Bandyopadhyay A., Beers T. C., Ezzeddine R., Sivarani T., Nayak P. K., Pandey J. C., Saraf P., Susmitha A., 2024, MNRAS, 529, 2191

Bestha M. et al., 2023, in Hull T.B., Kim D., Hallibert P., eds, Proc. SPIE Conf. Ser. Vol. 12677, Astronomical Optics: Design, Manufacture, and Test of Space and Ground Systems IV. SPIE, Bellingham, p. 126770Q

Bestha M. et al., 2024, in Bryant J. J., Motohara K., Vernet J. R. D., eds, Proc. SPIE Conf. Ser. Vol. 13096, Ground-based and Airborne Instrumentation for Astronomy X. SPIE, Bellingham, p. 1309661
Bestha M., Unni A., Sivarani T. R. D. S., Manickavasaham L. M. P., Divakar D. K., Surya A., 2025, in Ruane G. J., Millar-Blanchaer M. A., eds, Proc. SPIE Conf. Ser. Vol. 13627, Techniques and Instrumentation for Detection of Exoplanets XII. SPIE, Bellingham, p. 136271H
Birkby J. L., 2018, preprint (arXiv:1806.04617)
Cunningham C., Evans C., Monnet G., Le Louarn M., 2008, in Andersen T. E., ed., Proc. SPIE Conf. Ser. Vol. 6986, Extremely Large Telescopes: Which Wavelengths? Retirement Symposium for Arne Ardeberg. SPIE, Bellingham, p. 69860K
Eisenberg S., Shu K.-L., 1985, Appl. Opt., 24, 3944
Filippenko A. V., 1982, PASP, 94, 715
Giggenbach D., 2011, Appl. Opt., 50, 222
Greggio D., Schwab C., Magrin D., Filippo S. D., Viotto V., Rigaut F., 2020, in Evans C. J., Bryant J. J., Motohara K., eds, Proc. SPIE Conf. Ser. Vol. 11447, Ground-based and Airborne Instrumentation for Astronomy VIII. SPIE, Bellingham, p. 1144755
Harris R. J. et al., 2025, MNRAS, 536, 2421
Hill V. et al., 2002, A&A, 387, 560
Hohenkerk C. Y., Sinclair A. T., 1985, Technical report, NAO Technical Note
Johnson T. P., Sasian J., 2020, Appl. Opt., 59, G19
Kopon D., Close L. M., Gasho V., 2008, in Hubin N., Max C. E., Wizinowich P. L., eds, Proc. SPIE Conf. Ser. Vol. 7015, Adaptive Optics Systems. SPIE, Bellingham, p. 70156M
Leviton D. B., Frey B. J., Madison T. J., 2015, Temperature-dependent refractive index measurements of optical glasses. Technical report, NASA/TM-2015-218206, NASA Goddard Space Flight Center, https://ntrs.nasa.gov/api/citations/20150015986/downloads/20150015986.pdf (Accessed December 2025)
LLC R. Z., 2011, ZEMAX Optical Design Program User's Manual. https://neurophysics.ucsd.edu/Manuals/Zemax/ZemaxManual.pdf (Accessed December 2025)
Nikon, 2021, I-Line E Report. https://www.nikon.com/business/components/assets/pdf/i-line-e.pdf (Accessed December 2025)
Ohara Corporation, 2024, https://oharacorp.com/glass/pbl6y/ PBL6Y Optical Glass Data. (Accessed December 2025)
Oliva E., Tozzi A., Ferruzzi D., Riva M., Genoni M., Marconi A., Maiolino R., Origlia L., 2018, in Evans C. J., Simard L., Takami H., eds, Proc. SPIE Conf. Ser. Vol. 10702, Ground-based and Airborne Instrumentation for Astronomy VII. SPIE, Bellingham, p. 107028O
Padovani P., Cirasuolo M., 2023, Contemp. Phys., 64, 47
Parvathy M., Sivarani T., Sriram S., Bestha M., Divakar D. K., Rajaguru S. P., Surya A., 2025, in Hull T. B., Kim D., Hallibert P., eds, Proc. SPIE Conf. Ser. Vol. 13624, Astronomical Optics: Design, Manufacture, and Test of Space and Ground Systems V. SPIE, Bellingham, p. 1362422
Phillips A. C., Suzuki R., Larkin J. E., Moore A. M., Hayano Y., Tsuzuki T., Wright S. A., 2016, in Evans C. J., Simard L., Takami H., eds, Proc. SPIE Conf. Ser. Vol. 9908, Ground-based and Airborne Instrumentation for Astronomy VI. SPIE, Bellingham, p. 9908A1
Rakich A., 2021, Appl. Sci., 11, 6261
Rocha M. C., Goncharov A. V., 2022, Opt. Exp., 30, 6076
Rukdee S., 2024, Sci. Rep., 14, 27356
Santos N. C. et al., 2020, A&A, 644, A51
Saraf P., Prieto C. A., Sivarani T., Bandyopadhyay A., Beers T. C., Susmitha A., 2023, MNRAS, 524, 5607
SCHOTT, 2022, SCHOTT Optical Glass Data. https://media.schott.com/api/public/content/cea4f74030c245d58bfc22ff8a9bc075?v=aeab1d08 (Accessed December 2025)
Simcoe R. A., Furesz G., Egan M., Malonis A., Hellickson T., 2016, in Evans C. J., Simard L., Takami H., eds, Proc. SPIE Conf. Ser. Vol. 9908, Ground-based and Airborne Instrumentation for Astronomy VI. SPIE, Bellingham, p. 9908AA
Sinharoy I., 2014, Pyzdde: Python Zemax Dynamic Data Exchange toolbox. Zenodo, Geneva, Switzerland (Accessed December 2025)
Sivarani T. et al., 2004, A&A, 413, 1073
Sivarani T. et al., 2022, J. Astrophys. Astron., 43, 86
Smith W. J., 2023, Modern Optical Engineering: The Design of Optical Systems, 4th edn. McGraw Hill, New York
Sneden C., Johnson J., Kraft R. P., Smith G. H., Cowan J. J., Bolte M. S., 2000, ApJ, 536, L85
Spanò P., 2014, in Navarro R., Cunningham C. R., Barto A. A., eds, Proc. SPIE Conf. Ser. Vol. 9151, Advances in Optical and Mechanical Technologies for Telescopes and Instrumentation. SPIE, Bellingham, p. 915157
Su D.-q., Jia P., Liu G., 2012, MNRAS, 419, 3406
Szokoly G. P., 2005, A&A, 443, 703
Virtanen P. et al., 2020, Nat. Methods, 17, 261
Wang J. J., Wallace J. K., Jovanovic N., Guyon O., Roberts M., Mawet D., 2020, in Evans C. J., Bryant J. J., Motohara K., eds, Proc. SPIE Conf. Ser. Vol. 11447, Ground-based and Airborne Instrumentation for Astronomy VIII. SPIE, Bellingham, p. 1144754
Wehbe B., Cabral A., Ávila G., 2019, in Costa M. F. P. C. M. M., ed., Proc. SPIE Conf. Ser. Vol. 11207, Fourth International Conference on Applications of Optics and Photonics. SPIE, Bellingham, p. 112070P
Wehbe B., Cabral A., Martins J. H. C., Figueira P., Santos N. C., Ávila G., 2020a, MNRAS, 491, 3515
Wehbe B., Cabral A., Ávila G., 2020b, MNRAS, 499, 183
Wynne C. G., 1996, MNRAS, 282, 863
Wynne C. G., Worswick S. P., 1986, MNRAS, 220, 657
Zerbi F. M. et al., 2014, in Ramsay S. K., McLean I. S., Takami H., eds, Proc. SPIE Conf. Ser. Vol. 9147, Ground-based and Airborne Instrumentation for Astronomy V. SPIE, Bellingham, p. 914723

This paper has been typeset from a TEX/LATEX file prepared by the author.